Optics & Laser Technology 163 (2023) 109383

Contents lists available at ScienceDirect

Optics and Laser Technology

journal homepage: www.elsevier.com/locate/optlastec

Full length article

Analysis and experiment of polarization characteristics of Off-axis freeform optical system

Haodong Shi [a], Han Zhao [a], Jiayu Wang [a], Yi-Lan Zhang [b,*], Yufang Wu [a], Chao Wang [a], Qiang Fu [a], Huilin Jiang [a]

[a] Changchun University of Science and Technology, State Key Laboratory of Applied Optics, National and Local Joint Engineering Research Center for Space Optoelectronics Technology, Changchun 130022, China
[b] Southwest Institute of Technical Physics, Chengdu 610041, China

ARTICLE INFO

Keywords:
Jones matrix
Freeform surface
Polarized ray tracing
Polarized aberration
Off-axis system

ABSTRACT

As freeform surfaces are widely used in off-axis optical systems with large apertures, large fields of view, and long focal lengths, the polarization effect caused by the system cannot be ignored. For this in mind, a polarization aberration analysis method for freeform optical system with fringe Zernike polynomial is proposed. An analytical model for the polarization aberration in this case is constructed. The influence of the surface shape on the polarization aberration is investigated. Our analysis shows that the distribution of phase aberration, diattenuation and retardance at the exit pupil introduced by the freeform surface in the system is related to the entrance pupil, incident field angle, and also closely dependent on the surface sag of the freeform surface. The introduction of freeform surfaces causes the system polarization aberration distribution to lose rotational symmetry. Finally, a freeform surface multi-angle polarization characteristic test platform was built to test the validity of the theoretical model. The polarization aberration characteristic data of the incident mirror at different angles of view at different positions were obtained and analyzed. The measured results show that the relative errors of phase aberration, diattenuation and retardance are all less than 7.2%, which is basically consistent with the theoretical simulation analysis results. The research in this paper provides a theoretical basis for guiding the design of an off-axis freeform surface polarization imaging optical system, and provides theoretical guidance for improving the polarization aberration calibration of a freeform surface optical system.

1. Introduction

In recent years, polarization imaging has emerged as a promising means of optical detection, enabling high accuracy measurements of relevant information about imaged targets. It offers numerous advantages including background noise suppression, improvement of detection distance, acquisition of detailed features, and identification of camouflaged targets. Owing to this interesting set of features, a comprehensive, in-depth exploration of desired targets is achievable in polarization imaging. Furthermore, freeform surface imaging breaks through the limitations of traditional optical surfaces because of their non-rotational symmetry. Therefore, it is widely used in off-axis optical systems with large fields of view, large apertures, and long focal lengths [1–2]. Nonetheless, the influence of the non-rotationally symmetrical polarization aberration in the freeform surface imaging cannot be ignored[3].

In 1987, Russell A. Chipman proposed the polarization aberration theory, and decomposed the diattenuation and retardance aberration through the eigenvalues of the Jones matrix[4]. In 1994, James P. decomposed and expanded the polarization aberration function into a polarization aberration matrix, and performed polarization aberration analysis on a rotationally symmetric system[5]. The relationship between the polarization characteristics of the system and the field of view, pupil and wavelength is characterized by sets of mathematical function expressions. In recent years, numerous works have been reported on the investigation of polarization aberration. In 2019, Jeffrey M. Davis conducted a theoretical study on the polarization properties of coronagraphs[6]. The effect of polarization aberrations on the ability of coronagraphs to suppress on-axis starlight was analyzed. It was shown that, in the absence of adaptive optics, both isotropic and anisotropic polarization aberrations reduce the ability of coronagraphs to suppress starlight. In 2020, Luo Jing et al. demonstrated that the polarization

* Corresponding author.
E-mail address: 673258464@qq.com (Y.-L. Zhang).

https://doi.org/10.1016/j.optlastec.2023.109383
Received 25 October 2022; Received in revised form 23 January 2023; Accepted 13 March 2023
Available online 30 March 2023

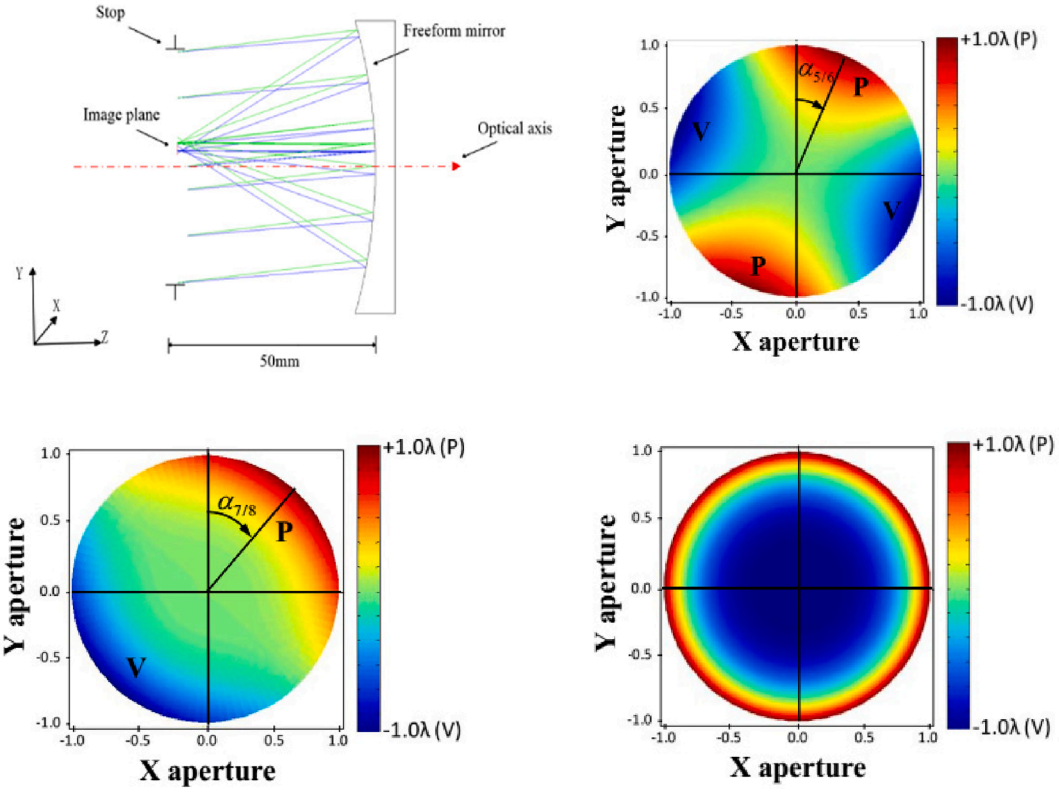

Fig. 1. Single-mirror system structure and freeform surface sag maps (a) system structure (b) $Z_{5/6}$ term, (c) $Z_{7/8}$ term, and (d) Z_9 term.

aberration of the unobstructed off-axis telescope has a non-negligible effect on its point spread function (PSF) optical ellipticity[7]. So far, most investigations focused on the analysis of the polarization characteristics of the inherent system. However, the analysis and modeling of the polarization aberration characteristics of the off-axis freeform optical system have remained scarce. This is mainly due to the difficulties associated with analyzing and mastering the distribution characteristics and laws of polarization aberrations in freeform optical systems. It is difficult for designers to optimize the distribution of polarization aberrations in optical systems in the early design stages, which greatly limits the application of polarization in high-precision space optical systems. Therefore, studying the polarization aberration distribution characteristics of off-axis freeform optical systems is of critical importance. In 2021, Yilan Zhang et al. proposed a polarization aberration analysis method based on the Jones notation using the fringe Zernike polynomials freeform surface. This research helps improving further the theoretical system of polarization aberrations[8]. On the other hand, it presents an important guiding significance for the application of freeform surfaces in polarization imaging systems.

In this study, we first demonstrate the construction of an analytical model for the polarization aberration of freeform surface optical system, based on Jones representation, using fringe Zernike polynomial as the characterization function. The influence of the freeform surface on the distribution characteristics of the diattenuation and retardance is analyzed. In addition, the theoretical system of the polarization aberration of the freeform surface is further improved. Second, we develop a test platform for multi-angle polarization characteristics and verify it through experiments. The Jones matrix of each sampling point on the freeform mirror at different field angles was measured, and the measured value of the polarization aberration on the freeform mirror with full aperture was calculated. Finally, measurement results are compared to simulations for the polarization aberration corresponding to different field angles of freeform surface obtained by optical design software. The correctness of the theory on the polarization aberration of freeform surface is thus verified.

2. Theory and method

This section focuses on the relative changes in the phase and amplitude of polarized light in optical systems. Compared to the Muller matrix, the Jones representation offers a more intuitive expression of the relationship between phase aberration, diattenuation, retardance, and freeform surfaces. Therefore, the polarization theory based on the Jones vector and Jones matrix has been adopted in this study[9–11].

2.1. Phase aberration modeling

Zernike polynomials have strong ability to fit the global surface shape of non-rotationally symmetric surfaces. They are usually used to characterize the surface features of freeform surfaces. The phase aberration introduced by the Zernike polynomial freeform surface in the coaxial system is related to the surface sag, which can be expressed as [8]:

$$\phi_0(\vec{\boldsymbol{H}},\vec{\boldsymbol{\rho}},\lambda)=\frac{2\pi}{\lambda}\frac{(n_2-n_1)}{\lambda}\sqrt{C_x^2+C_y^2}e^{ima_{x/y}}\cdot Z\left(\vec{\boldsymbol{\rho}}+\Delta\vec{\boldsymbol{h}}\right)$$
$$=\frac{2\pi}{\lambda}\vec{\boldsymbol{V}}_{x/y}\cdot Z\left(\vec{\boldsymbol{\rho}}+\Delta\vec{\boldsymbol{h}}\right) \quad (1)$$

where $\vec{\boldsymbol{H}}$ denotes a normalized vector for the field height in the image plane, and $\vec{\boldsymbol{\rho}}$ denotes a normalized vector describing the position in the pupil, Z denotes the Zernike polynomial freeform surface sag, n_1 and n_2 are the refractive indices of the medium where the incident and outgoing rays are located, λ is the wavelength, and C_x and C_y are a set of Zernike polynomial coefficients. $\alpha_{x/y}$ represents the direction of the coefficient vector, where $\alpha_{x/y}$ has been modified. It is specified to represent the clockwise rotation angle from the Y-axis direction in the right-handed coordinate system, which is defined as: $\alpha_{x/y}=$

$\frac{\pi}{2}-\frac{1}{m}\arctan\left(\frac{C_y}{C_x}\right)$. m represents a multiple of the Zernike polynomial azimuth ϕ, whereas $\Delta\vec{h}$ is a pupil offset vector when the freeform surface is located away from the stop.

For small field of view angles, the offset vector has a linear relationship with the field of view, which can be expressed as:

$$\Delta\vec{h}=\left(\frac{\bar{y}}{y}\right)\vec{H} \tag{2}$$

where y and $\bar{y}$ represent the edge ray height and the incident chief ray height of the off-axis field of view, respectively.

When the stop is located on the freeform surface, the value of y is equal with $\bar{y}$. In this case, under the same aperture, the area of the incident light on the freeform surface is the same for each field of view. Moreover, the surface shape has the same effect on the light for each field of view. Therefore, the phase aberration contribution produced by the freeform surface in this case is independent of the field of view. When the stop position is far away from the freeform surface, the phase aberration distribution generated by the freeform surface will change with the field of view, since $\Delta\vec{h}$ is related to the field of view vector $\vec{H}$. In order to analyze the influence of the freeform surface on the phase aberration distribution when the freeform surface is at any position in the optical system, we derive, in the following, the phase aberration analytical formula for the freeform surface far from the stop position.

When the freeform surface is far away from the stop position, the aperture of the light irradiated on the freeform surface will be shifted. Thus, the aperture shift vector $\Delta\vec{h}$, and phase aberration contribution of the freeform surface will correspondingly become[8]:

$$\phi_0(\vec{H},\vec{\rho},\lambda)=\frac{2\pi}{\lambda}\vec{\delta}_{x/y}(\vec{\rho})\ =\ \frac{2\pi}{\lambda}\vec{V}_{x/y}\cdot Z\left(\vec{\rho}+\Delta\vec{h}\right) \tag{3}$$

It can be seen from equation (3) that, although the Zernike polynomial is only related to the aperture, its aberration contribution may also be related to the field of view when it is far away from the stop position.

For a specific analysis of the phase aberration distribution characteristics introduced by the freeform surface, the first nine distributions of the Zernike polynomial will be analyzed and discussed below. Among them, the first three are pure phase changes, which have no effect on the imaging quality. The fourth item represents the defocus, which can be eliminated by adjusting the position of the image plane. Therefore, in this study, we analyze the distribution characteristics of the introduced phase aberration one by one starting from item 5. When the freeform surfaces $Z_{5/6}$、$Z_{7/8}$ and Z_9 items are far away from the diaphragm, the expression of the phase aberration ϕ_0 is[8]:

$$\begin{cases}
\phi_{0,5/6,nonstop}\left(\vec{H},\vec{\rho},\lambda\right)=\frac{2\pi}{\lambda}\cdot\vec{\delta}_{5/6,nonstop} \\
=\frac{2\pi}{\lambda}\left[\vec{V}_{5/6}\cdot\vec{\rho}^{2}+2\left(\frac{\bar{y}}{y}\right)\vec{V}_{5/6}\vec{H}^{*}\cdot\vec{\rho}+\left(\frac{\bar{y}}{y}\right)^{2}\vec{V}_{5/6}\vec{H}^{2}\right] \\
\phi_{0,7/8,nonstop}\left(\vec{H},\vec{\rho},\lambda\right)=\frac{2\pi}{\lambda}\cdot\vec{\delta}_{7/8,nonstop} \\
=\frac{2\pi}{\lambda}\left[3\vec{V}_{7/8}\cdot\left(\vec{\rho}+\Delta\vec{h}\right)\right]\left[\left(\vec{\rho}+\Delta\vec{h}\right)\cdot\left(\vec{\rho}+\Delta\vec{h}h\right)\right] \\
=\frac{2\pi}{\lambda}\left[\begin{array}{c}3\left(\vec{V}_{7/8}\cdot\vec{\rho}\right)(\vec{\rho}\cdot\vec{\rho})+3\left(\frac{\bar{y}}{y}\right)\left(\vec{V}_{7/8}\vec{H}\cdot\vec{\rho}^{2}\right)+3\left(\frac{\bar{y}}{y}\right)^{2}\left(\vec{H}\cdot\vec{H}\right)\left(\vec{V}_{7/8}\cdot\vec{\rho}\right)+ \\ 6\left(\frac{\bar{y}}{y}\right)(\vec{\rho}\cdot\vec{\rho})\left(\vec{V}_{7/8}\cdot\vec{H}\right)+6\left(\frac{\bar{y}}{y}\right)^{2}\left(\vec{V}_{7/8}\cdot\vec{H}\right)\left(\vec{H}\cdot\vec{\rho}\right)+3\left(\frac{\bar{y}}{y}\right)^{3}\left(\vec{H}\cdot\vec{H}\right)\left(\vec{V}_{7/8}\cdot\vec{H}\right)\end{array}\right] \\
\phi_{0,9,nonstop}\left(\vec{H},\vec{\rho},\lambda\right)=\frac{2\pi}{\lambda}\cdot\vec{\delta}_{9,nonstop} \\
=\frac{2\pi}{\lambda}\cdot 6V_9\left[\left(\vec{\rho}+\Delta\vec{h}\right)\cdot\left(\vec{\rho}+\Delta\vec{h}\right)\right]^{2} \\
=\frac{2\pi}{\lambda}\left[\begin{array}{c}6V_9(\vec{\rho}\cdot\vec{\rho})^{2}+12V_9\left(\frac{\bar{y}}{y}\right)^{2}\left(\vec{H}^{2}\cdot\vec{\rho}^{2}\right)+6V_9\left(\frac{\bar{y}}{y}\right)^{4}\left(\vec{H}\cdot\vec{H}\right)^{2}+24V_9\left(\frac{\bar{y}}{y}\right)\left(\vec{H}\cdot\vec{\rho}\right)(\vec{\rho}\cdot\vec{\rho}) \\ +24V_9\left(\frac{\bar{y}}{y}\right)^{3}\left(\vec{H}\cdot\vec{H}\right)\left(\vec{H}\cdot\vec{\rho}\right)+24V_9\left(\frac{\bar{y}}{y}\right)^{2}\left(\vec{H}\cdot\vec{H}\right)(\vec{\rho}\cdot\vec{\rho})\end{array}\right]
\end{cases} \tag{4}$$

where $\vec{V}_{5/6}=\frac{(n_2-n_1)}{\lambda}\sqrt{C_5^2+C_6^2}e^{i2\alpha_{5/6}},\alpha_{5/6}=\frac{\pi}{2}-\frac{1}{2}\arctan\left(\frac{C_6}{C_5}\right)$, $\vec{V}_{7/8}=\frac{(n_2-n_1)}{\lambda}\sqrt{C_7^2+C_8^2}e^{i2\alpha_{7/8}},\alpha_{7/8}=\frac{\pi}{2}-\arctan\left(\frac{C_8}{C_7}\right)$, and $V_9=C_9$ is a scalar.

In order to analysis the polarization aberration distribution of a freeform surface, a single-mirror system with freeform surface was built. The spherical radius of the mirror is 100 mm, the off-axis field of view angle is from 2° to 4° and the aperture stop is placed at a distance of 50 mm from the front of the mirror. The optical path of the system is shown in Fig. 1(a). Then different Zernike parameters are introduced independently, such as the $Z_{5/6}$-term, $Z_{7/8}$-term and Z_9-term of the freeform surface with Zernike coefficient of λ, respectively. The freeform surface sag with different Zernike terms are shown in Fig. 1(b)-(d). The optical design software and Matlab are used to trace the full-aperture polarized ray of the single-mirror system. The effect of the freeform surface $Z_{5/6}$、$Z_{7/8}$ and Z_9 terms on the phase aberration is obtained, as shown in Fig. 2. It can be seen that the phase aberration distribution in the pupil is consistent with the sagittal height map of the freeform surface, with zero at the pupil center. The distribution of phase aberrations introduced by

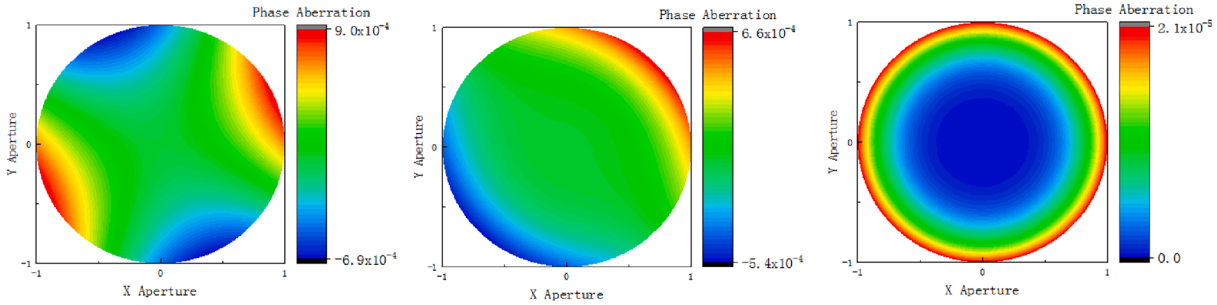

Fig. 2. Influence of Zernike polynomial (a) $Z_{5/6}$ term, (b) $Z_{7/8}$ term, and (c) Z_9 term freeform surface on the polarization aberration of the system.

the $Z_{5/6}$-term and $Z_{7/8}$-term freeform surfaces are plane-symmetrical in the pupil, whereas that induced by the Z_9-term is rotationally symmetric.

2.2. Diattenuation and retardance modeling

Traditionally, two-dimensional polarization ray tracing[6,12–15] is employed, which uses the Jones matrix to characterize the polarization properties of the optical interface[16–17]. However, since the normal vector of each point on the freeform surface is different, the direction of the emitted ray corresponding to different light incidence angles, is also different. Adding the light propagation vector $\vec{k}$ to the traditional two-dimensional matrix can improve the analysis of the polarization properties of optical systems containing freeform surfaces.

The Jones matrix is added to the propagation vector $\vec{k}$ as a 3×3 matrix $\boldsymbol{P_q}$, which represents the change in the polarization state when light passes through each interface of the optical system.

The relationship between $\boldsymbol{P_q}$ and the $\vec{k}$, $\vec{s}$ and $\vec{p}$ components of the light beam at the optical interface is

$$\boldsymbol{P_q} = \begin{pmatrix} s_{x,q} & p_{x,q} & k_{x,q} \\ s_{y,q} & p_{y,q} & k_{y,q} \\ s_{z,q} & p_{z,q} & k_{z,q} \end{pmatrix} \begin{pmatrix} a_{s,q} & 0 & 0 \\ 0 & a_{p,q} & 0 \\ 0 & 0 & 1 \end{pmatrix} \begin{pmatrix} s_{x,q-1} & s_{y,q-1} & s_{z,q-1} \\ p_{x,q-1} & p_{y,q-1} & p_{z,q-1} \\ k_{x,q-1} & k_{y,q-1} & k_{z,q-1} \end{pmatrix} \tag{5}$$

where $a_{s,q}$ and $a_{p,q}$ are the amplitude transmission (reflection) coefficients of the $\vec{s}$ and $\vec{p}$ components of the q-th interface, respectively.$s_{m,q-1}$, $p_{m,q-1}$, and $k_{m,q-1}(m = x,y,z)$ represent the coordinates of the $\vec{s}$, $\vec{p}$ and $\vec{k}$ components of the incident light in the global coordinate system, respectively, whereas $s_{n,q}$, $p_{n,q}$, $k_{n,q}(n = x,y,z)$ represent the coordinates of the $\vec{s}$, $\vec{p}$ and $\vec{k}$ components of the emerging light. The $\vec{s}$ and $\vec{p}$ components can be calculated using by

$$\vec{s}_{q-1} = \frac{\vec{k}_{q-1} \times \vec{k}_q}{\left|\vec{k}_{q-1} \times \vec{k}_q\right|}, \vec{p}_{q-1} = \vec{k}_{q-1} \times \vec{s}_{q-1}, \vec{s}_q = \vec{s}_{q-1}, \vec{p}_q = \vec{k}_q \times \vec{s}_q \tag{6}$$

Taking the j-th surface in the optical system as an example, a freeform surface is added to the system, whose expression is given by:

$$z = \frac{cr^2}{1 + \sqrt{1 - (1+k)c^2r^2}} + \sum_{i=1}^{M} C_i Z_i(\rho, \phi) \tag{7}$$

where c is the spherical curvature, k is the conic coefficient, r is the radial aperture, and C_i is the Zernike coefficient corresponding to the i term of the Zernike polynomial. The normal vector of the freeform surface can be expressed as

$$n = \begin{bmatrix} n_x \\ n_y \\ n_z \end{bmatrix} = \frac{1}{\sqrt{\left(\frac{\partial z}{\partial x}\right)^2 + \left(\frac{\partial z}{\partial y}\right)^2 + 1}} \begin{bmatrix} \frac{\partial z}{\partial x} \\ \frac{\partial z}{\partial y} \\ -1 \end{bmatrix} \tag{8}$$

When the light is reflected on the mirror with the normal line $\begin{bmatrix} n_x & n_y & n_z \end{bmatrix}^T$, the transformation matrix of the light propagation direction is given by

$$H = \begin{bmatrix} 1-2n_x^2 & -2n_xn_y & -2n_xn_z \\ -2n_xn_y & 1-2n_y^2 & -2n_yn_z \\ -2n_xn_z & -2n_yn_z & 1-2n_z^2 \end{bmatrix} = \frac{1}{\left(\frac{\partial z}{\partial x}\right)^2 + \left(\frac{\partial z}{\partial y}\right)^2 + 1} \begin{bmatrix} -\left(\frac{\partial z}{\partial x}\right)^2 + \left(\frac{\partial z}{\partial y}\right)^2 + 1 & -2\frac{\partial z}{\partial x} \times \frac{\partial z}{\partial y} & 2\frac{\partial z}{\partial x} \\ -2\frac{\partial z}{\partial x} \times \frac{\partial z}{\partial y} & \left(\frac{\partial z}{\partial x}\right)^2 - \left(\frac{\partial z}{\partial y}\right)^2 + 1 & 2\frac{\partial z}{\partial y} \\ 2\frac{\partial z}{\partial x} & 2\frac{\partial z}{\partial y} & \left(\frac{\partial z}{\partial x}\right)^2 + \left(\frac{\partial z}{\partial y}\right)^2 - 1 \end{bmatrix}, \tag{9}$$

Following the passage of the propagation vector $k_{in} = \begin{bmatrix} k_{in,x} & k_{in,y} & k_{in,z} \end{bmatrix}^T$ through the optical system, the expression of the transmission vector of the outgoing light becomes

$$\boldsymbol{k_{out}} = \begin{bmatrix} k_{out,x} \\ k_{out,y} \\ k_{out,z} \end{bmatrix} = H \cdot \boldsymbol{k_{in}} = \frac{1}{\left(\frac{\partial z}{\partial x}\right)^2 + \left(\frac{\partial z}{\partial y}\right)^2 + 1} \begin{bmatrix} \left[-\left(\frac{\partial z}{\partial x}\right)^2 + \left(\frac{\partial z}{\partial y}\right)^2 + 1 \right] k_{in,x} + \left(-2\frac{\partial z}{\partial x} \times \frac{\partial z}{\partial y} \right) k_{in,y} + \left(2\frac{\partial z}{\partial x} \right) k_{in,z} \\ \left(-2\frac{\partial z}{\partial x} \times \frac{\partial z}{\partial y} \right) k_{in,x} + \left[\left(\frac{\partial z}{\partial x}\right)^2 - \left(\frac{\partial z}{\partial y}\right)^2 + 1 \right] k_{in,y} + \left(2\frac{\partial z}{\partial y} \right) k_{in,z} \\ \left(2\frac{\partial z}{\partial x} \right) k_{in,x} + \left(2\frac{\partial z}{\partial y} \right) k_{in,y} + \left[\left(\frac{\partial z}{\partial x}\right)^2 + \left(\frac{\partial z}{\partial y}\right)^2 - 1 \right] k_{in,z} \end{bmatrix} \tag{10}$$

Then the expression of the incident angle is given by

$$\cos\theta_1 = \frac{\vec{n} \cdot \vec{k}_{in}}{|\vec{n}| \cdot \left|\vec{k}_{in}\right|} = \frac{\frac{\partial z}{\partial x} \cdot k_{in,x} + \frac{\partial z}{\partial y} \cdot k_{in,y} - k_{in,z}}{\sqrt{\left(\frac{\partial z}{\partial x}\right)^2 + \left(\frac{\partial z}{\partial y}\right)^2 + 1}} \tag{11}$$

For a ray obliquely incident on a metal interface:

$$\sin\theta_2 = \frac{1}{\tilde{n}} \sin\theta_1 \tag{12}$$

where $\tilde{n}$ represents the metal complex refractive index of the surface film, θ_2 is a complex number and is no longer a reflection angle in the traditional sense. The expressions for $a_{s,1}$ and $a_{p,1}$ are:

$$a_{s,1} = -\frac{\sin(\theta_1 - \theta_2)}{\sin(\theta_1 + \theta_2)}, a_{p,1} = \frac{\tan(\theta_1 - \theta_2)}{\tan(\theta_1 + \theta_2)} \tag{13}$$

According to Equation (6), the components of s and p are expressed as:

$$\boldsymbol{s}_0 = \boldsymbol{s}_1 = \begin{bmatrix} s_x \\ s_y \\ s_z \end{bmatrix}, \boldsymbol{p}_0 = \begin{bmatrix} p_{x,0} \\ p_{y,0} \\ p_{z,0} \end{bmatrix} = k_{in} \times \boldsymbol{s}_0, \boldsymbol{p}_1 = \begin{bmatrix} p_{x,1} \\ p_{y,1} \\ p_{z,1} \end{bmatrix} = k_{out} \times \boldsymbol{s}_1 \tag{14}$$

By Substituting into formula (5), and performing singular value decomposition on P, it could be verified that $a_{s,1}^2 \cdot \vec{s}_0 = (P^T \cdot P) \cdot \vec{s}_0, a_{p,1}^2 \cdot \vec{p}_0 = (P^T \cdot P) \cdot \vec{p}_0$. Therefore, $a_{s,1}$ and $a_{p,1}$ are the eigenvalues of matrix P.

According to the Taylor decomposition over the complex field, $a_{s,1}$ and $a_{p,1}$ can be expressed approximately as:

$$\begin{aligned} a_{s,1} &= -\frac{\sin(\theta_1 - \theta_2)}{\sin(\theta_1 + \theta_2)} \approx -\frac{(\theta_1 - \theta_2)\left[1 - \frac{1}{3!}(\theta_1 - \theta_2)^2 + \frac{1}{5!}(\theta_1 - \theta_2)^4\right]}{(\theta_1 + \theta_2)\left[1 - \frac{1}{3!}(\theta_1 + \theta_2)^2 + \frac{1}{5!}(\theta_1 + \theta_2)^4\right]}, \\ a_{p,1} &= \frac{\tan(\theta_1 - \theta_2)}{\tan(\theta_1 + \theta_2)} \approx \frac{(\theta_1 - \theta_2)\left(1 + \frac{1}{3}(\theta_1 - \theta_2)^2 + \frac{2}{15}(\theta_1 - \theta_2)^4\right)}{(\theta_1 + \theta_2)\left(1 + \frac{1}{3}(\theta_1 + \theta_2)^2 + \frac{2}{15}(\theta_1 + \theta_2)^4\right)}. \end{aligned} \tag{15}$$

By using (11), (12) in (15), we can get:

$$\begin{aligned} a_{s,1} &\approx -\frac{\tilde{n} - 1}{\tilde{n} + 1} \cdot \frac{1 - \frac{1}{3!}\left[\left(1 - \frac{1}{\tilde{n}}\right)Q\right]^2 + \frac{1}{5!}\left[\left(1 - \frac{1}{\tilde{n}}\right)Q\right]^4}{1 - \frac{1}{3!}\left[\left(1 + \frac{1}{\tilde{n}}\right)Q\right]^2 + \frac{1}{5!}\left[\left(1 + \frac{1}{\tilde{n}}\right)Q\right]^4} = |a_{s,1}|e^{i\varphi_{s,1}} \\ a_{p,1} &\approx \frac{\tilde{n} - 1}{\tilde{n} + 1} \cdot \frac{1 + \frac{1}{3}\left[\left(1 - \frac{1}{\tilde{n}}\right)Q\right]^2 + \frac{2}{15}\left[\left(1 - \frac{1}{\tilde{n}}\right)Q\right]^4}{1 + \frac{1}{3}\left[\left(1 + \frac{1}{\tilde{n}}\right)Q\right]^2 + \frac{2}{15}\left[\left(1 + \frac{1}{\tilde{n}}\right)Q\right]^4} = |a_{p,1}|e^{i\varphi_{p,1}} \end{aligned} \tag{16}$$

$$Q = \sqrt{2 - 2\frac{\frac{\partial z}{\partial x} \cdot k_{in,x} + \frac{\partial z}{\partial y} \cdot k_{in,y} - k_{in,z}}{\sqrt{\left(\frac{\partial z}{\partial x}\right)^2 + \left(\frac{\partial z}{\partial y}\right)^2 + 1}}}.$$

In formula (16), $a_{s,1}$ and $a_{p,1}$ are identified as functions of Zernike polynomial coefficients and incident light vector, respectively. According to the definition of diattenuation and retardance, we can get:

$$\begin{aligned} D &= \frac{|a_{s,1}|^2 - |a_{p,1}|^2}{|a_{s,1}|^2 + |a_{p,1}|^2}. \\ \delta &= \varphi_{s,1} - \varphi_{p,1}. \end{aligned} \tag{17}$$

Since diattenuation and retardance are related to $a_{s,1}$ and $a_{p,1}$, they are consequently related to the freeform surface. Therefore, the aforementioned arguments establish the theoretical model of diattenuation and retardance of freeform. It follows that, when the type of freeform surface is given, the diattenuation and retardance can be calculated using formula (17).

The polarization aberration distribution of a freeform surface single-mirror system is analyzed with the help of optical software, and the effects of the freeform surface $Z_{5/6}$,$Z_{7/8}$ and Z_9 items on the two-way attenuation and phase retardation are obtained, as shown in Figs. 3 and 4. It can be seen that the distribution of diattenuation and retardance in the pupil is consistent with the sagogram of the freeform surface.

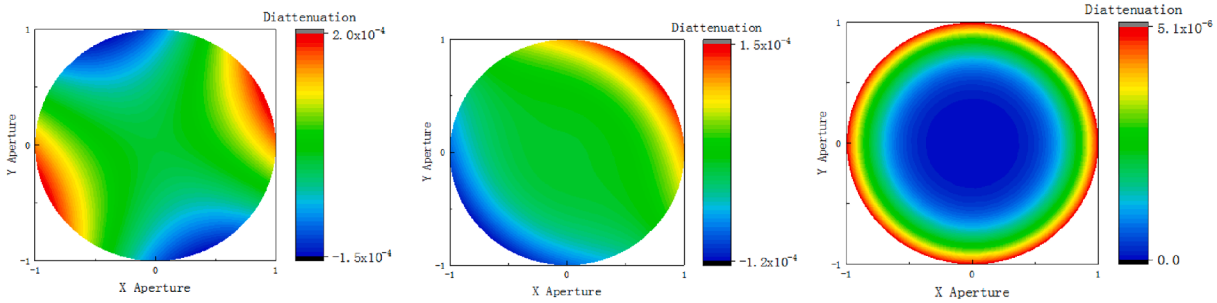

Fig. 3. Distribution of the diattenuation introduced by the $Z_{5/6}$, $Z_{7/8}$, and Z_9 coefficients of the Zernike polynomial freeform surface.

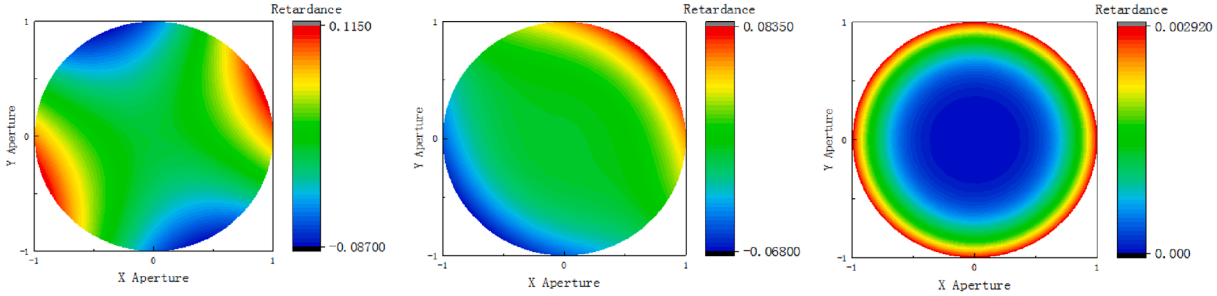

Fig. 4. Distribution of the retardance introduced by the $Z_{5/6}$, $Z_{7/8}$, and Z_9 coefficients of the Zernike polynomial freeform surface.

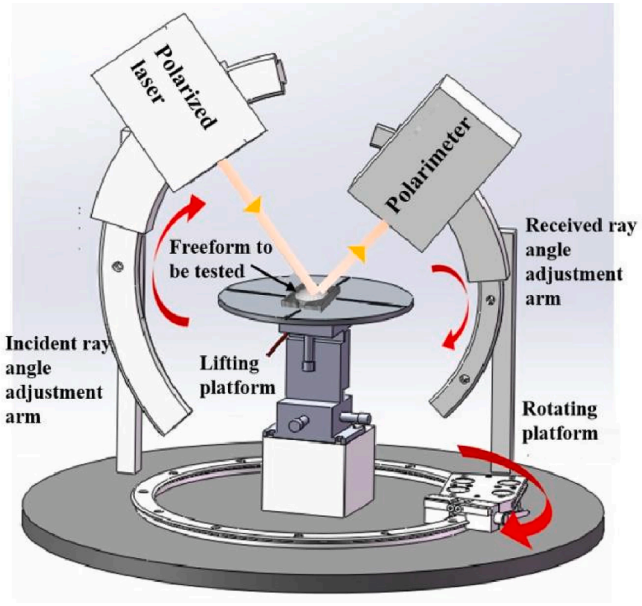

Fig. 5. Experimental diagram.

3. Experimental verification

We built an indoor freeform surface multi-angle polarization test platform, to use for verifying the correctness of our theoretical analysis results based on the polarization aberration model described above.

3.1. Experiment process

The design of the home-built test platform is shown in Fig. 5. The linear polarized light is emitted by the adjustable polarization state laser. The angle of the light incident on the mirror is adjusted by the angle adjustment arm to simulate the incident light of the edge field of view. Then the polarimeter is used to measure the polarization state of the light emitted by the mirror.

The finalized setup of the freeform surface multi-angle polarization test platform is shown in Fig. 6. A polarimeter (model: PAN5710VIS from THORLABS) is used to measure the polarization state of the outgoing light. During the experiment, the working wavelength of the polarization state measuring instrument was set to 633 nm, which corresponded to the wavelength of the laser used. The polarimeter was used to calibrate the outgoing light as linearly polarized light. The mechanical structure of the platform consists of two angle adjustment arms, used to control the pitch angle of the laser and the polarimeter through an electronic control system. A stage to accommodate the mirror to be measured is placed on a rotary support structure that enables the rotation on the sample.

During the polarization state measurement, instrument jitter and stray light interference will induce some deviations. These factors introduce a systematic error of the experimental test, which imposes the need to

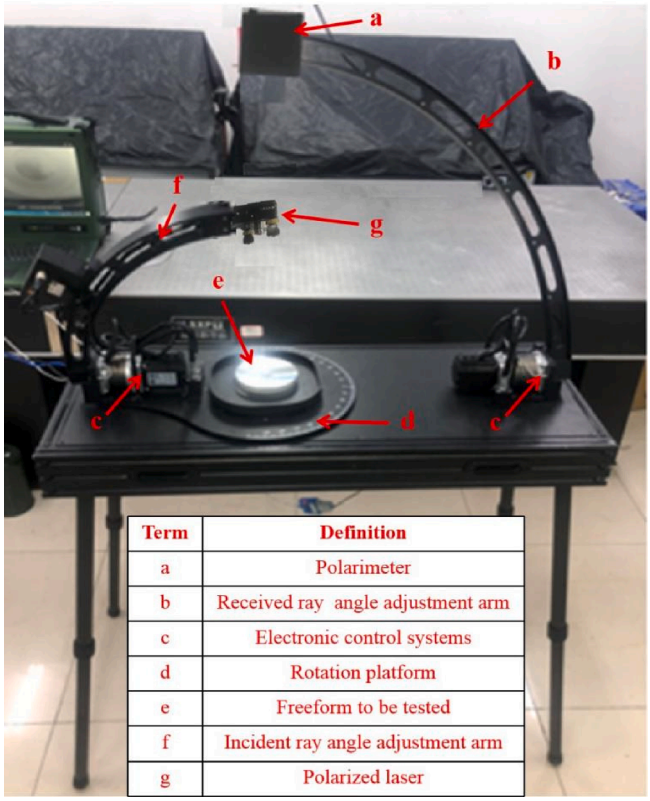

Term	Definition
a	Polarimeter
b	Received ray angle adjustment arm
c	Electronic control systems
d	Rotation platform
e	Freeform to be tested
f	Incident ray angle adjustment arm
g	Polarized laser

Fig. 6. Freeform surface multi-angle polarization test platform.

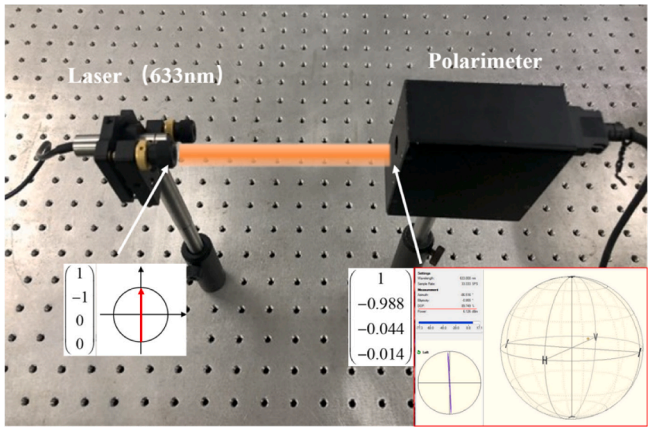

Fig. 7. Calibration of polarization state measuring instrument.

Table 1
Relative errors of three parameters obtained by measuring linearly polarized light in the vertical direction.

"Stokes 1″	"Stokes 2″	"Stokes 3″
0.022	−0.208	0.024
0.001	−0.036	0.020
0.017	−0.184	−0.006
0.024	−0.218	−0.001
0.019	−0.142	0.009
0.003	−0.074	0.015
0.004	−0.082	0.037

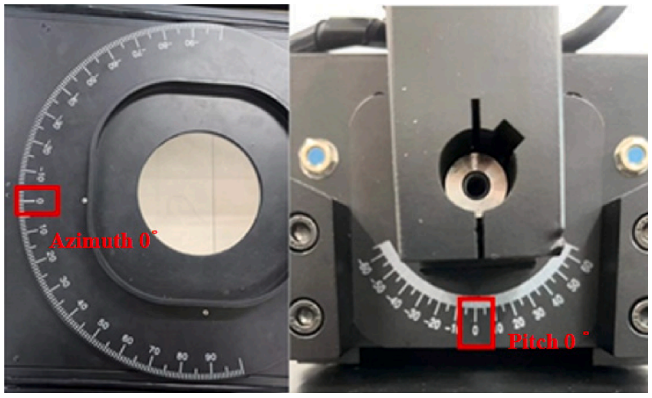

Fig. 8. Azimuth starting position and the pitch starting position.

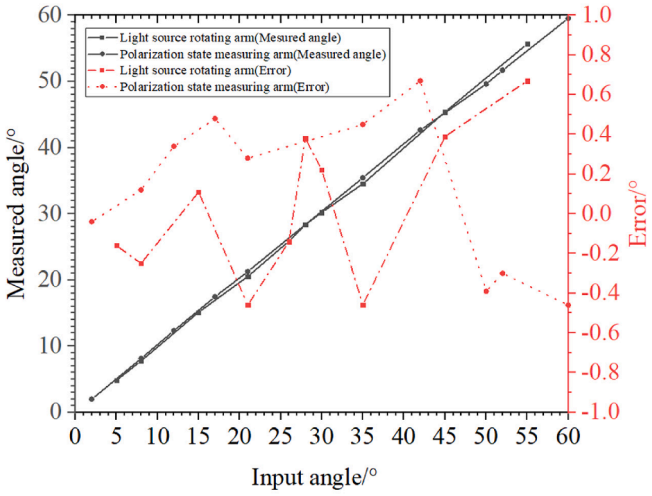

Fig. 9. Rotation angle calibration results of light source arm and polarization state measuring arm.

calibrate the accuracy of the polarization state measuring instrument prior to measurements. Moreover, when adjusting the arms to set a specified angle, deviations would be introduced due to factors such as mechanical and gear errors. This requires additional calibration of the angle adjustment accuracy for the angle adjustment arm of the test platform.

The Boncare sphere method and Stokes vector are expressed when measuring the polarization state. Thus, the calibration process is define as follows. First, the laser with adjustable polarization state emits linearly polarized light in the horizontal direction, and its polarization state is detected using a polarization state meter and is represented by the Stokes vector $[1 \quad 1 \quad 0 \quad 0]^T$. Similarly, the laser is used to emit vertically linearly polarized light, and its polarization state is represented by the Stokes vector $[1 \quad -1 \quad 0 \quad 0]^T$. For calibration, the polarized laser is experimentally measured in the two configurations above, as shown for

Fig. 10. Interferometer measures the freeform surface of the mirror.

Table 2
Freeform surface parameters.

Indicator	parameter
c	0.002042
k	0
C_1	-4.760×10^{-6}
C_2	3.394×10^{-6}
C_3	4.301×10^{-6}
C_4	4.922×10^{-7}
C_5	1.034×10^{-8}
C_6	-2.584×10^{-8}
C_7	-1.034×10^{-8}
C_8	7.358×10^{-12}
C_9	-1.589×10^{-7}

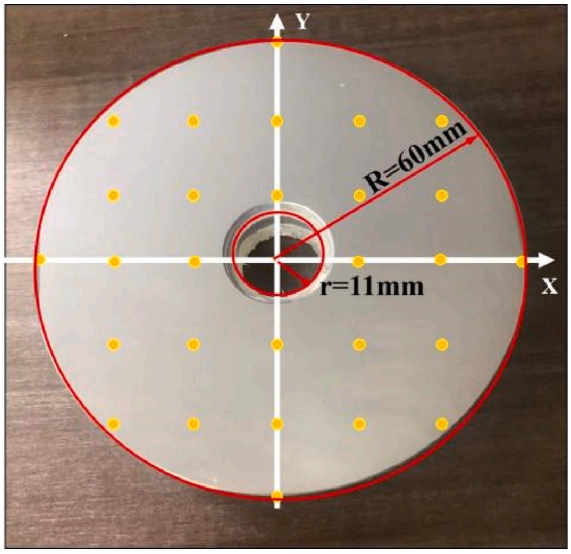

Fig. 11. Mirror sampling point distribution.

example in Fig. 7. In practice, the measured Stokes vector is normalized and is represented by the set of four S_0, S_1, S_2, S_3, where $S_0 = 1$ Fig. 7.

The goal of the calibration procedure is to determine the deviation between the theoretically expected values of the Stokes vector and the actually measured values in both the vertical and horizontal linear polarization cases.

While the first parameter $S_0 = 1$, the other three parameters S_1, S_2, S_3 correspond to Stokes 1, Stokes 2, and Stokes 3 in Table 1, showing the experimentally measured values for the case of vertically linearly polarized light. The differences in values with the expected ones are used

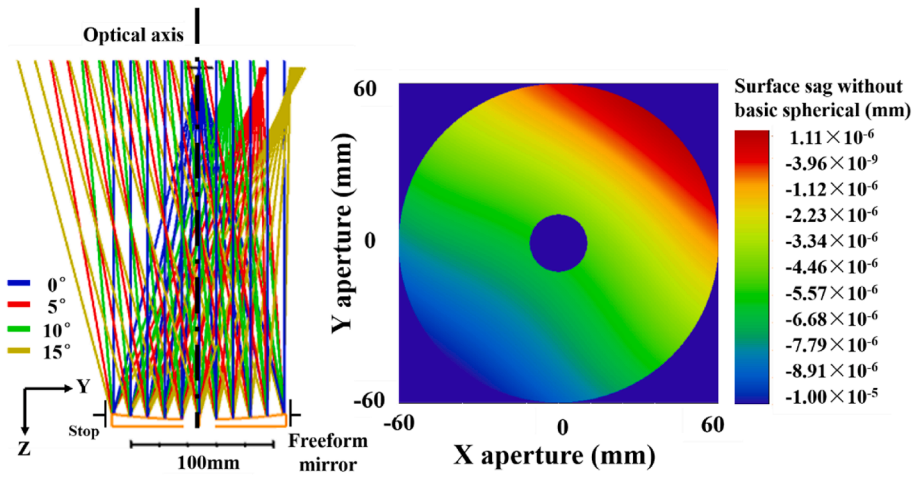

Fig. 12. Optical path diagram and freeform surface sagogram.

to calibrate the test platform. Thus, the measurement error of the polarization state measuring instrument can be eliminated by the calibrated relative error.

Azimuth starting position and the pitch starting position are shown in Fig. 8. A high-precision gyroscope is used to calibrate the angle adjustment arm for the measurement of the inclination angle. The calibration process consists in the following steps. First, the high-precision gyroscope is fixed at the horizontal position of the light source rotating arm. Second, the system control is turned on and the desired position is set. Finally, the observation and reading of the light source angle on the platform and the rotation angle on the gyroscope are compared. The calibration results are shown in Fig. 9. The maximum error of light source rotating arm is 0.67°and the maximum error of polarization state measuring arm is 0.66°. These errors can be eliminated by calibration procedure.

A freeform surface mirror with a spherical surface as the base was selected as a test sample for experimental measurements. The mirror is 120 mm in diameter and 22 mm in clear aperture, with the surface coated with an industrial aluminum film (over-coated by a protective layer). The freeform surface of the mirror can be fitted by using the ZYGO interferometer, as shown in Fig. 10. To represent the mirror surface type, the Zernike coefficients are read on the interferometer, and $z = \frac{cr^2}{1+\sqrt{1-(1+k)c^2r^2}} + \sum_{i=1}^{M} C_i Z_i(\rho, \phi)$ is used. The specific surface type parameters are shown in Table 2.

The mirror is placed on the test bench, where the center of the circle matches the origin; X- and Y-axes correspond to the horizontal and vertical directions, respectively. Uniformly distributed 29 sampling points are selected on the surface of the mirror, as shown in Fig. 11.

To validate the polarization aberration theoretical model introduced by the freeform surface, a single-mirror optical system of the freeform surface was established by ZEMAX software, as shown in Fig. 12. The Zernike coefficients of the freeform surface are shown in Table 2. The Jones matrix of each sampling point position on the pupil is obtained by polarized ray tracing, under the condition of a field angle of 0°, 5°, 10°, and 15°. The distribution of phase aberration on the pupil in a specific field of view is obtained by performing Pauli decomposition on each Jones matrix. The bidirectional attenuation and phase in a specific field of view is obtained using three-dimensional expansion and singular value decomposition on each Jones matrix.

Fig. 12 shows the result obtained using the ZEMAX software simulation. Next, the measured values of polarization aberrations at various points on the mirror will be obtained by applying our theoretical model and experimental measurements.

First, we select a sampling point and control the swing amplitude of the swing arm to $\beta(\beta = 0^{\circ})$, that is, we set the edge field of view to 0°. Then, the propagation vector $\vec{k}_{in}$ of the incident beam can be expressed as:

$$\vec{k}_{in} = [k_{in,x} \quad k_{in,y} \quad k_{in,z}]^T = [0 \quad \sin\beta \quad -\cos\beta] \tag{18}$$

where, $k_{in,x}$、$k_{in,y}$、$k_{in,z}$ represent the coordinates of the incident light vector on the ×, y, and z axes, respectively. Given the Zernike representation of the surface shape of the freeform surface, the expression of the normal vector n of the freeform surface is:

$$n = \begin{bmatrix} n_x \\ n_y \\ n_z \end{bmatrix} = \frac{1}{\sqrt{\left(\frac{\partial z}{\partial x}\right)^2 + \left(\frac{\partial z}{\partial y}\right)^2 + 1}} \begin{bmatrix} \frac{\partial z}{\partial x} \\ \frac{\partial z}{\partial y} \\ -1 \end{bmatrix}, \tag{19}$$

where, n_x、n_y、n_z represent the coordinates of the incident light vector on the ×, y, and z axes, respectively. After the propagation vector $k_{in} = [0 \quad \sin\beta \quad -\cos\beta]^T$ of the incident beam passes through the optical system, the transmission vector expression of the outgoing light is:

$$\vec{k}_{out} = \begin{bmatrix} k_{out,x} \\ k_{out,y} \\ k_{out,z} \end{bmatrix} = \boldsymbol{H} \cdot \vec{k}_{in} = \frac{1}{\left(\frac{\partial z}{\partial x}\right)^2 + \left(\frac{\partial z}{\partial y}\right)^2 + 1} \begin{bmatrix} \left[-\left(\frac{\partial z}{\partial x}\right)^2 + \left(\frac{\partial z}{\partial y}\right)^2 + 1\right] k_{in,x} + \left(-2\frac{\partial z}{\partial x} \times \frac{\partial z}{\partial y}\right) k_{in,y} + \left(2\frac{\partial z}{\partial x}\right) k_{in,z} \\ \left(-2\frac{\partial z}{\partial x} \times \frac{\partial z}{\partial y}\right) k_{in,x} + \left[\left(\frac{\partial z}{\partial x}\right)^2 - \left(\frac{\partial z}{\partial y}\right)^2 + 1\right] k_{in,y} + \left(2\frac{\partial z}{\partial y}\right) k_{in,z} \\ \left(2\frac{\partial z}{\partial x}\right) k_{in,x} + \left(2\frac{\partial z}{\partial y}\right) k_{in,y} + \left[\left(\frac{\partial z}{\partial x}\right)^2 + \left(\frac{\partial z}{\partial y}\right)^2 - 1\right] k_{in,z} \end{bmatrix} \tag{20}$$

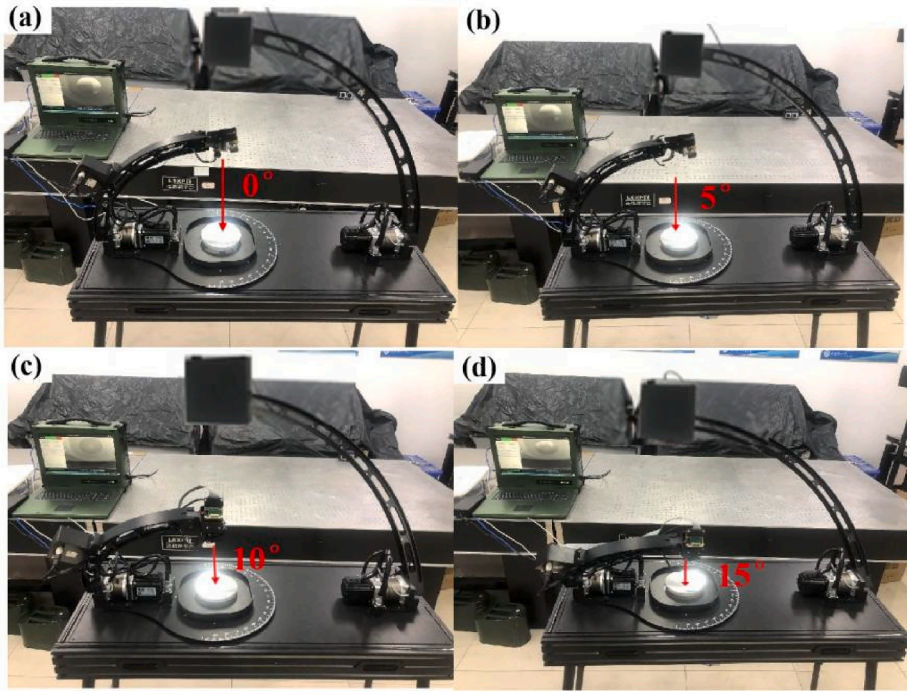

Fig. 13. Polarization aberration measurement under different field of view conditions.

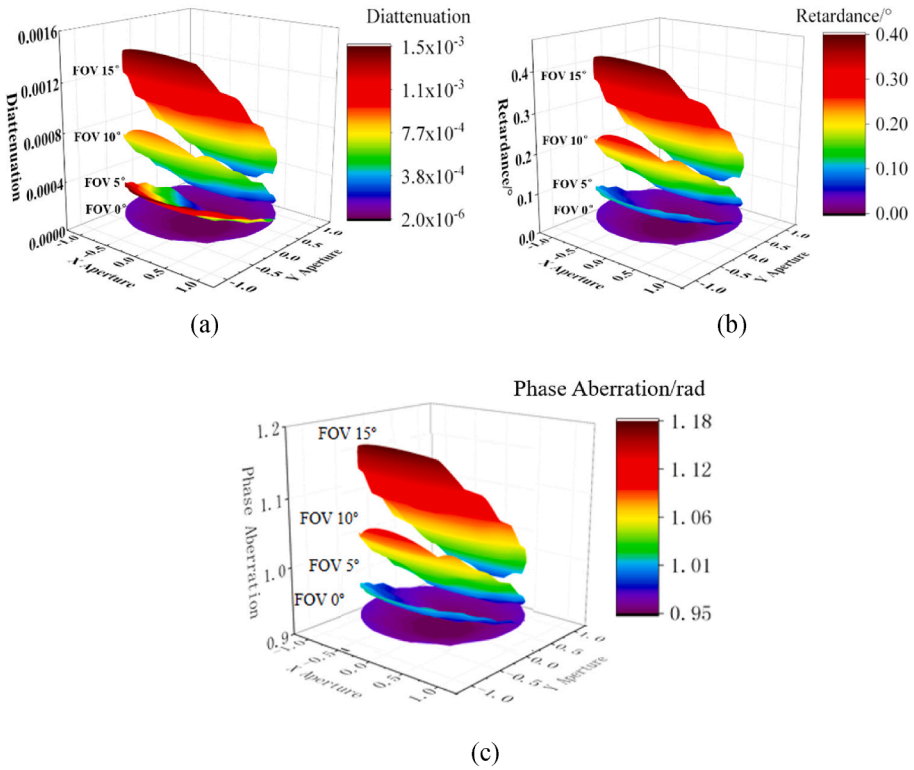

Fig. 14. The magnitude of polarization aberration measured by ZEMAX simulation under different field of view conditions. (a) Distribution of full aperture of diattenuation under different FOV conditions (b) Distribution of full aperture of retardance under different FOV conditions (c) Distribution of full aperture of phase aberration under different FOV conditions.

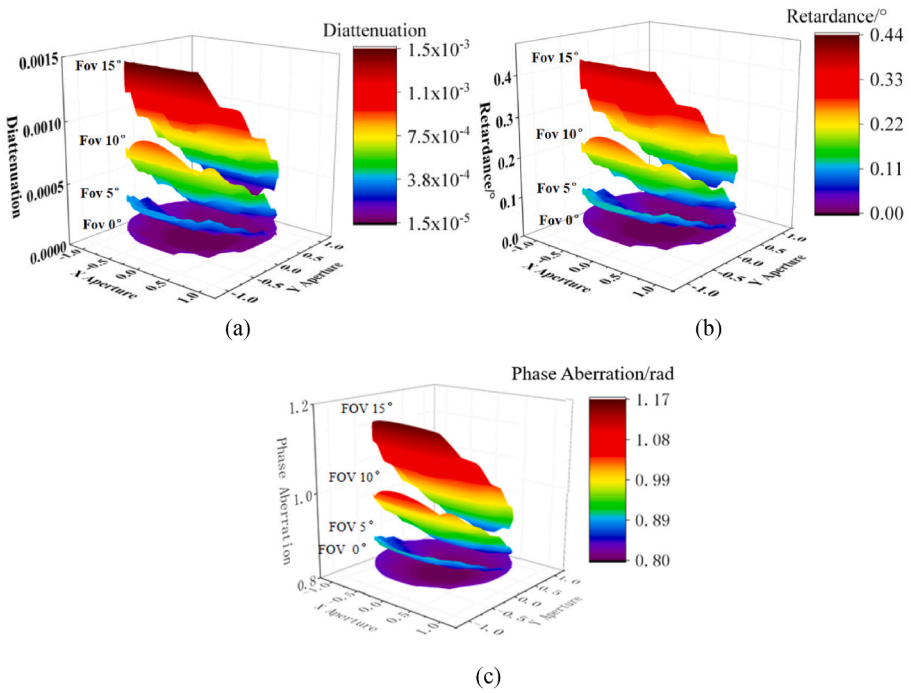

Fig. 15. The magnitude of polarization aberration under different FOV conditions calculated by experiment and theoretical model. (a) Distribution of full aperture of diattenuation under different FOV conditions (b) Distribution of full aperture of retardance under different FOV conditions (c) Distribution of full aperture of phase aberration under different FOV conditions.

Then the expression for the cosine of the incident angle is:

$$\cos\theta_1 = \frac{\vec{n}\cdot\vec{k}_{in}}{|\vec{n}|\cdot|\vec{k}_{in}|} = \frac{\frac{\partial z}{\partial x}k_{in,x} + \frac{\partial z}{\partial y}k_{in,y} - k_{in,z}}{\sqrt{\left(\frac{\partial z}{\partial x}\right)^2 + \left(\frac{\partial z}{\partial y}\right)^2 + 1}} \tag{21}$$

According to formula (17), the diattenuation and retardance of this point under the condition of the field of view can be obtained. This sets the determination of diattenuation and retardance value of the pupil point through the theoretical model.

Next, the test platform is used to experimentally measure the phase aberration. The Jones matrix of the freeform surface mirror is set to be $\boldsymbol{J} = \begin{bmatrix} A & B \\ C & D \end{bmatrix}$, wherein A, B, C, and D represent the four parameters. The measurement protocol is defined as follows. First, a point is selected, and then the swing arm and the fringe field of view are both set at 0°. The incident beam is calibrated as horizontally polarized light by the polarization state measuring instrument, and the polarization state of the incident light is $\vec{E}_{in,X} = \begin{bmatrix} 1 \\ 0 \end{bmatrix}$, then the polarization state of the outgoing light is determined by

$$\vec{E}_{out,X} = \boldsymbol{J}\cdot\vec{E}_{in,X} = \begin{bmatrix} A & B \\ C & D \end{bmatrix}\cdot\begin{bmatrix} 1 \\ 0 \end{bmatrix} = \frac{1}{\sqrt{A^2 + C^2}}\begin{bmatrix} A \\ C \end{bmatrix}. \tag{22}$$

Afterwards, the incident beam is calibrated as vertically polarized light, where the polarization state of the incident light is: $\vec{E}_{in,Y} = \begin{bmatrix} 0 \\ 1 \end{bmatrix}$. Then, the polarization state of the outgoing light determined by

$$\vec{E}_{out,Y} = \boldsymbol{J}\cdot\vec{E}_{in,Y} = \begin{bmatrix} A & B \\ C & D \end{bmatrix}\cdot\begin{bmatrix} 0 \\ 1 \end{bmatrix} = \frac{1}{\sqrt{B^2 + D^2}}\begin{bmatrix} B \\ D \end{bmatrix} \tag{23}$$

The above protocol is repeated for several rounds to reduce the operation error. Based on this, the Jones matrix of the point under the condition of a field angle is obtained. And Pauli decomposition is performed on it to obtain the corresponding phase aberration. The next step consists in adjusting the swing arm for different field of view angles, i.e. 5°, 10°, and 15°, as shown in Fig. 13. And then, the aforementioned protocol to determine the corresponding phase aberration, diattenuation, and retardance of the point for each case is applied.

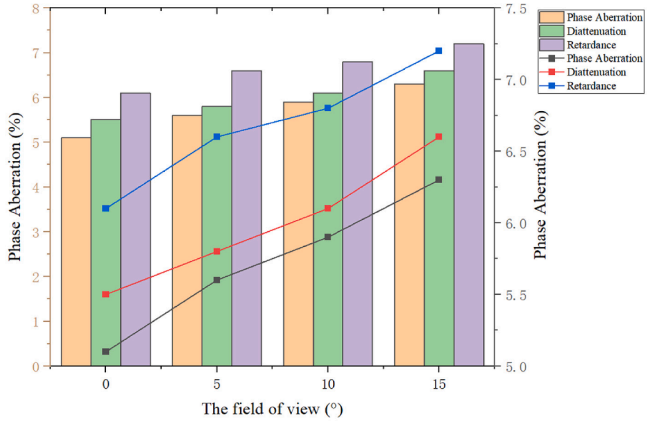

Fig. 16. Relative error between the measured value and the simulated value under different FOV conditions.

3.2. Experimental results and analysis

To verify the correctness of the theory developed here, a comparison is drawn between the experimental measurements and simulated values obtained by ZEMAX. Following the protocol described in the previous section, Fig. 14 shows the results for the magnitude and distribution of polarization aberration determined at each point through simulations by ZEMAX.

The changing trends of diattenuation, retardance and phase aberration are noticeably the same, similar to the vector map of the freeform surface of the mirror. The increase of the angle of view will increase the polarization aberration of the system. Under the condition of the same angle of view, the position of the pupil is different, and the introduction of the freeform surface will deflect the normal of the incident light, which is no longer directed to the center of the standard sphere. Thus, the incident angle is affected by the surface shape of the freeform surface, which in turn affects the distribution of polarization aberrations in the full aperture. Polarization aberration is influenced by the field of view, pupil position, and freeform surface shape.

Fig. 15 shows the experimentally measured polarization aberration at each point on the mirror.

The distribution of the full-aperture diattenuation, retardance, and phase aberration in each field of view is calculated by the above theoretical model. This is consistent with the polarization aberration trend obtained by building a reflection system with ZEMAX optical software and performing real ray tracing on it. Thus, the correctness of the freeform surface polarization aberration model is verified.

The relative errors between the measured and simulated values under different field of view angles are shown in Fig. 16.

Clearly, as the field of view is increased, a larger error is induced in the measured value of polarization aberration. The relative error for the phase aberration is 6.3%, for diattenuation 6.6%, and for retardance 7.2%.

This is attributed to a combined effect of random errors including:

1. A film system error: there is a deviation between the theoretically simulated film system and the actual measured film system;
2. An error generated by the instrument: which occurs in case jitter, pull, stretching or squeezing happen during experiments. The incident light is no longer the standard X (Y) linearly polarized light, which will affect the polarization state of the outgoing light.
3. An error caused by the environment: which manifest by the influence of external stray light and other factors during experimental verification.

The existence of random errors will lead to some deviations in the experimentally measured data, which will subsequently affect the Jones matrix and polarization aberration obtained.

4. Conclusion

In this study, a theoretical model for the polarization aberration of the off-axis optical system with freeform surface was established by introducing the Zernike polynomial freeform surface into the system. The influence of the freeform surface on the polarization aberration distribution of the off-axis system was investigated. An experimental test platform for multi-angle polarization characteristics of a freeform surface was built. By controlling the incident angle of a specific polarized light, the polarization state of the outgoing light was measured, and the polarization aberration data of the full field of view and full-aperture of a single freeform surface mirror was obtained. Following a detailed calibration procedure described in this study, the experimental values were compared to the theory to validate our proposed theoretical model.

The introduction of Zernike polynomial freeform surface, to elaborate the theoretical model for the system, can meet the technical requirements of large aperture, large field of view, and long focal length. Nevertheless, our findings show that this infers polarization aberration, dependent on the surface shape of the freeform surface.

Funding

This work was supported by the Natural Science Foundation of Jilin Province (YDZJ202301ZYTS417) and National Science Foundation of China (NSFC), grant numbers 61890960, 61805027 and 61805028.

CRediT authorship contribution statement

Haodong Shi: Conceptualization, Formal analysis, Visualization, Writing – original draft, Project administration. **Han Zhao:** Writing – review & editing. **Jiayu Wang:** Validation, Supervision. **Yi-Lan Zhang:** Methodology, Validation, Resources. **Yufang Wu:** Formal analysis. **Chao Wang:** Investigation. **Qiang Fu:** Data curation. **Huilin Jiang:** Funding acquisition.

Declaration of Competing Interest

The authors declare that they have no known competing financial interests or personal relationships that could have appeared to influence the work reported in this paper.

Data availability

The data that has been used is confidential.

References

[1] M. Beier, J. Hartung, T. Peschel, et al., Development, Fabrication, and Testing of an Anamorphic Imaging Snap-together Freeform Telescope, Appl. Opt. 54 (12) (2015) 3530–3542.
[2] K. Fuerschbach, G.E. Davis, K.P. Thompson, et al., Assembly of a Freeform Off-axis Optical System Employing Three φ-Polynomial Zernike Mirrors, Opt. Lett. 39 (10) (2014) 2896–2899.
[3] J. Luo, X.u. Chenxu You, X.Z. He, Comparisons between an on-axis three-mirror anastigmat telescope and an off-axis one: polarization aberrations, Appl. Opt. 60 (22) (2021) 6438–6447.
[4] R.A. Chipman, Polarization aberrations, The University of Arizona, 1987.
[5] J.P. Mcguire, R.A. Chipman, Polarization aberrations.1 Rotationally symmetric optical systems, Appl. Opt. 33 (22) (1994) 5080.
[6] J.M. Davis, Polarization Aberrations in Coronagraphs, The University of Arizona, 2019.
[7] J. Luo, X.U. He, K. Fan, et al., Effects of polarization aberrations in an unobscured off-axis space telescope on its PSF ellipticity, Opt. Express 28 (25) (2020).
[8] Y. Zhang, H. Shi, H. Jiang, Polarization Aberration of a Non-Rotationally Symmetric Optical System With Freeform Surfaces, IEEE Access 9 (2021) 145538–145553.
[9] J.P. Mcguire, R.A. Chipman, Polarization aberrations. 2. Tilted and decentered optical systems, Appl. Opt. 33 (22) (1994) 5101.
[10] R.A. Chipman, Polarization analysis of optical systems, Int. Soc. Opt. Eng. 28 (2) (1989) 090.
[11] R.A. Chipman, Mechanics of polarization ray tracing, Opt. Eng. 34 (6) (1995) 1636.
[12] S. Michael, I. Shinya, O. Rudolf, Polarization aberrations caused by differential transmission and phase shift in high-numerical-aperture lenses: theory, measurement, and rectification, Opt. Eng. 41 (5) (2002) 943.
[13] R.A. Chipman, L.J. Chipman, polarization aberration diagrams, Opt. Eng. 28 (2) (1989) 100.
[14] E. Li, Y. Li, Y. Liu, et al., Rigorous imaging-based measurement method of polarization aberration in hyper-numerical aperture projection optics, Opt. Eng. 29 (13) (2021) 20872.
[15] Y.B. Liao, Polarization Optics, Science Press, Beijing, 2003, pp. 45–63.
[16] G. Yun, K. Crabtree, R.A. Chipman, Three-dimensional polarization ray-tracing calculus I definition and diattenuation, Appl. Opt. 50 (18) (2011) 2855.
[17] T. Li, Y. Liu, Y. Sun, et al., Vectorial pupil optimization to compensate polarization distortion in immersion lithography system, Opt. Express 28 (4) (2020).